19th Australasian Fluid Mechanics Conference
Melbourne, Australia
8-11 December 2014

Tracking Blood Drops Ejected from the Nasal Cavity during Violent Assault

P.H. Geoghegan[1*], C.J.T. Spence[2], N. Kabaliuk[1], J. Aplin[1], J. Wilhelm[1], M.C. Taylor[3] and M.C. Jermy[1]

[1]Department of Mechanical Engineering
University of Canterbury, Christchurch, Canterbury 8041, New Zealand

[2]Fisher & Paykel Healthcare Ltd
Auckland 1741, New Zealand

[3]Institute of Environmental Science and Research (ESR)
Christchurch, Canterbury 8041, New Zealand

Abstract

Expirated blood is blood released from the mouth or nose which leaves characteristic stains at crime scenes which may convey valuable information about the disposition of assailant and victim. Little work has been done to determine the typical velocities and trajectories of the droplets which make such patterns. Stereoscopic Particle Image Velocimetry (SPIV) and a model of the human upper airway were used to measure the velocity field near the nostrils during exhalation. The trajectories of blood drops emerging from the nose were computed with a numerical model. For an expiration flow rate of 32 l/min in vivo there is a maximum exit velocity from the nostril of approximately 4 m/s. From a height of 1.7 m blood drops between 0.5 mm and 2 mm reach terminal velocity. Their exit velocity at the nostril does not affect impact velocity, but it does influence impact location. Drop size affects both impact location and impact velocity. Compared to the 2 mm drop, the 0.5 mm drop had a reduced impact velocity, but its impact location in the ground plane was further from the nostril exit. Understanding the physics of expirated blood flight allows better interpretation of expirated stains on different surfaces at crime scenes.

Introduction

Bloodstain pattern evidence is often crucial in police investigations and in judicial trials, but is sometimes misinterpreted, with serious consequences: juries unable to reach the correct verdict, coroners unable to determine if a death is suicide or murder, and cases retried due in large part to confusion over bloodstain evidence [1-3, 5, 11]. This confusion arises from a lack of fundamental understanding of the complex physical processes that generate blood stains [4] and a lack of science-based, peer-reviewed methods for interpreting bloodstain evidence [7]. In New Zealand, there are on average 86.1 homicides per year, with 93% resolved the same year (a suspect arrested, but not necessarily convicted). There are approximately 35,000 "Acts intended to harm" each year (84% resolved) (averages taken over 2003-2012, [6]). Only 44% of homicide prosecutions and 58% of acts intended to cause injury result in convictions (averaged over 2002-2011, [6]). There are clearly opportunities to improve detection and make better objective use of evidence in court to resolve more violent crimes.

An important class of bloodstain patterns arises from expirated blood, i.e. blood expelled from the nose and/or mouth as the victim breathes out or coughs. Currently, the range of initial velocities of these droplets is poorly known. The droplet size, velocity and impact angle determine the characteristics of the stain resulting from impact on a nearby surface. The present work determines the velocity field in front of the nose during exhalation using SPIV and a refractive matched silicone flow phantom. This data provides the exit velocity a blood drop will possess as it leaves the nasal cavity. The subsequent blood drop trajectory and impact angle can be calculated using a computer model developed in-house [14] that solves the droplet equation of motion and uses empirical correlations to determine the drag coefficient of aerodynamically deformed (nonspherical) droplets. This information is important in understanding the information encoded in bloodstains at the crime scene, which may contribute to scene reconstruction by determining the locations of the victim and assailant when the crime was committed. An understanding of the physics of expirated blood drop flight is also important in determining the limits of certainty of the information extracted from the bloodstain pattern. The certainty (or otherwise) of the inferences made from stain patterns are critical in determining whether stain evidence can contribute to a conviction. Little experimental analysis has been performed in this area [8, 9].

Experimental Methodology

The geometry of the nasal cavity was from CT data of a 44-year-old male and comprised 452 axially acquired 512 × 512 pixel^2 images with 0.6 mm slice spacing and thickness. In-plane pixel size was 0.42 × 0.42 mm. The nasal cavity was declared free of any visible abnormalities by a radiologist. The model includes both sides of the nasal cavity and extends to the beginning of the trachea. Features such as nostril hairs and the mucous layer inside the nasal cavity were not resolved because the main interest of this paper was the large scale flow features external of the nasal cavity, which were assumed independent of these details.

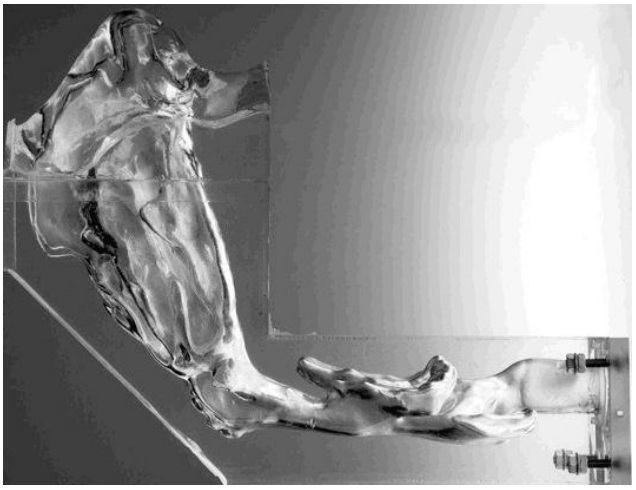

Figure 1. Silicone nasal cavity flow phantom viewed sagittally from the right

A 1.55 times life size rigid transparent silicone flow phantom (Figure 1) [15] was produced by rapid prototyping the CT scan data in a water dissoluble material and embedding this in a clear silicone resin. After the resin had cured, the model was removed, leaving a transparent scaled flow phantom of the nasal cavity [10]. The final silicone model was itself CT scanned and found to deviate by a mean of 0.32 mm (on a 1:1 (in-vivo) scale) from the original segmented CT data.

The phantom was attached to the flow system shown in Figure 2. Glycerol (61% w/w) and water (39% w/w) was used as the flow medium, matching the refractive index (1.43) of the phantom at 25°C. Temperature was maintained with a cooling and heating system. The reservoir tank (b) was filled to a depth such that the free surface showed minimal movement, ensuring that at the in vivo steady expiration flow rate of 32 l/min (realistic expiratory air flow rate when naturally exhaling air) there was a constant exit pressure at the nose. Flow rate control was controlled by a ball valve and electromagnetic flow meter (c) (Sparling Tigermag FM626). Dimensionally similar in-vitro flow rates were obtained by matching the Reynolds number in the nasopharynx (equation (1)), where Q is the flow rate and ν is the kinematic viscosity. Experimental parameters are shown in Table 1.

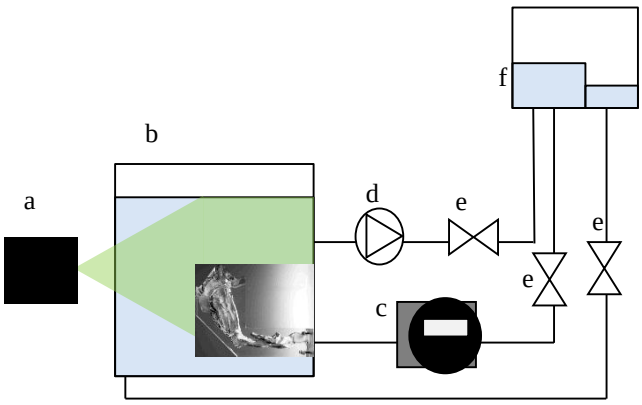

Figure 2. Layout of the experimental setup (a) laser and optics (b) reservoir containing silicone flow phantom (c) electromagnetic flow meter (d) return pump (e) ball valves for flow control (f)) header tank with weir to ensure constant pressure

$$Q_{invitro} = 1.55 \frac{\nu_{invitro}}{\nu_{invivo}} Q_{invivo} \quad (1)$$

	In Vivo	In Vitro
ρ (kg/m^3)	1.068	1154
μ (kg/ms)	1.846x10^{-5}	9.27x10^{-3}
Flowrate (l/min)	32	22.78
Velocity (m/s)	2.6	0.77
Inlet Re	2228	2228

Table 1. In vivo and in vitro experimental flow parameters

The SPIV system consisted of a 15-Hz dual-head 120 mJ Nd:YAG laser (New Wave Solo 120XT), two digital 2 Mpixel CCD cameras (Dantec Flowsense) and optics to form a light sheet of approximately 2 mm thickness. The flow was seeded with near neutrally buoyant 10 μm hollow silver coated spheres, such that approximately nine particles were contained within the final interrogation window size. Laser and camera timings were synchronised using a BNC 565 pulse delay generator. To take advantage of the Lorenz-Mie scatter pattern the left camera was positioned at a small stereo angle of -2.3º and the right camera positioned at 30.4º in forward scatter. A minimum background subtraction technique was applied. Images were processed with a dynamic histogram filter and Gaussian smoothing with a 3 × 3 kernel. This resulted in a wider correlation peak, improving the sub-pixel fitting and peak locking that is normally associated with under sampled images. The Gaussian filter also acted as a low pass filter and removed high frequency noise such as CCD noise. A zero flow condition was applied to the non-flow regions by way of a masking technique with masks obtained from the CT scan of the flow phantom, extracting the cross-sections at measurement planes analysed using Paraview [10].

Camera calibrations were made at each measurement plane with a self-calibration routine applied to correct for misalignments. Correlation was performed on an initial window size of 64 × 64 pix^2 using an iterative window refinement technique to 32 × 32 pix^2. An average overlap factor of 74% was obtained using a grid spacing of 1.2 mm. Window deformation and displacement were also applied. The light sheet and CCD cameras were fixed and the reservoir traversed in increments of 2 mm to obtain 22 sagittal slices per phantom. Mean flow fields and a reconstructed volume were produced from ensemble correlation averaging 245 image pairs. Time delays ranged from 650-1500 μs through the planes to ensure a maximum particle displacement of about 8 pixels in any one plane.

Computational Methodology

A description of the computational model used to track the blood drops through the velocity field obtained from the SPIV results can be found in [12]. The code incorporated gravitational and aerodynamic drag forces as well as in-flight drop deformation, oscillations and secondary break-up. The developed numerical scheme is able to predict drop 3D coordinates, velocity along the flight trajectory, impact angle and velocity, distance travelled and drop aspect ratio. The blood drops were modelled using a Lagrangian approach, by applying Newton's Second Law to an individual drop travelling through air (equation 2). The set of 1st order ODE for drop velocity components were solved each time step using a 4th order Runge-Kutta numerical method. An initially spherical drop may reach maximum deformation when it takes the form of a disk. The drag coefficient of a deformed drop can thus be estimated by interpolating between that of a sphere and of a disk using equation 3. The empirical expressions for the drag coefficient of a solid sphere and disk for a wide range of Reynolds numbers can be found in [12]. The code was extensively validated against experimental and analytical data [12].

$$m\vec{a} = m\vec{g} + \frac{\pi}{6} d_0^3 \rho_a \vec{g} - \frac{1}{2} C_d A \rho_a V_{rel}^2 \frac{\vec{V}_{rel}}{\left|\vec{V}_{rel}\right|} \quad (2)$$

$$C_D = AR \cdot C_D^{Sph} + (1 - AR) C_D^{Disk} \quad (3)$$

Drops are tracked in the in vivo scaled velocity field from the nostril exit to a ground plane set 1.7 m below (representative of the average nose height of an adult male). The blood density and surface tension was 1056 kg/m^3 and 0.062 N/m (at 37 °C) respectively. Blood drops were assumed to have zero initial velocity as they left the skin surface and were then in turn carried and accelerated by the stream of air. The trajectory tracking model took the initial conditions from the velocity magnitude and direction at the nostril exit. The droplet displacement was then calculated at time steps of 0.001 s through the flow field accounting for velocity magnitude and direction changes as it moved.

Results

Figure 3 presents the in vivo absolute velocities in the central plane of the two jets exiting the nostrils of the nasal cavity obtained using SPIV. Velocities below 0.6m/s have been removed from the image as these lay outside the exiting jet streams. The peak exit velocity varies between the two nostrils with the left and right nostril having a peak exit velocity of 3.47 and 3.96 m/s, respectively. The cause of this difference in exit velocity can be seen in Figure 4 which shows there to be an asymmetry through the nasal cavity geometry. This means that the exit flow field from the nostrils will vary between victims and will require an understanding of the geometry to predict the flow field. It is also highly likely that blood exiting the nostril during a crime is released by a blow to the nasal region and this should be taken into consideration.

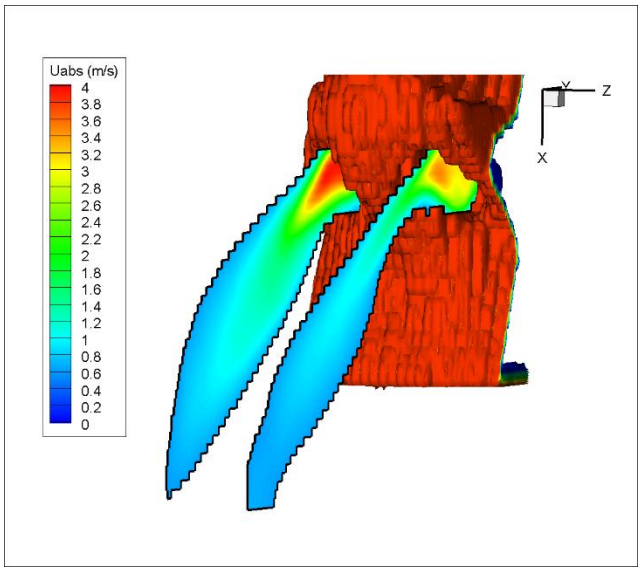

Figure 3. Absolute velocities through the central planes of the jets exiting through the nostrils (orange iso-surface represents the external surface of the nose and upper lip)

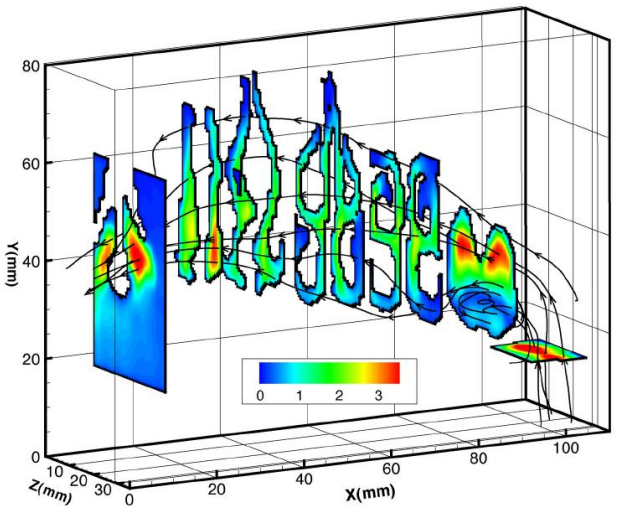

Figure 4. Absolute velocities through the nasal cavity terminating at the nostrils

Figure 5 shows the results for a blood drop with diameter 2mm exiting the right (a) and left (b) nostril and the trajectory it follows through the jet. After the drop exits the jet boundary shown in Figure 3 the computer model tracks the drop until it impacts with the ground. The main forces acting from here are gravity and drag. Ambient conditions such as draughts, cross winds etc. have not been incorporated in this current analysis.

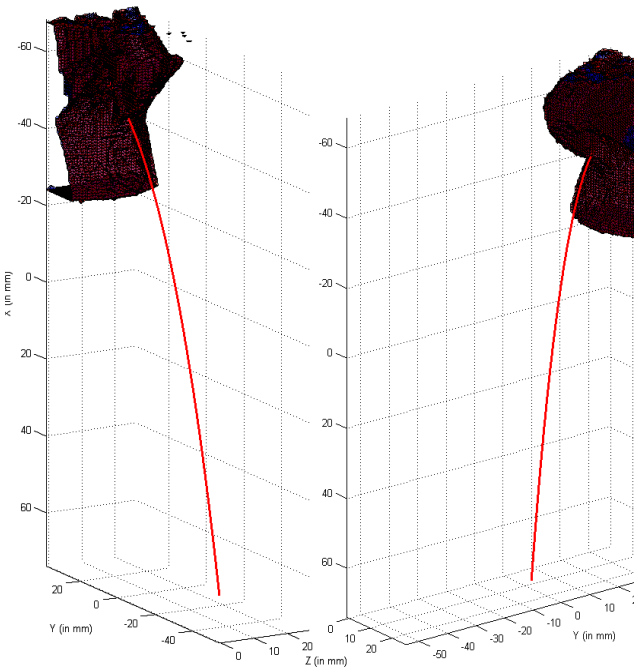

Figure 5. Predicted blood drop trajectory of a 2mm blood drop within the jet exiting from (a) the right nostril and (b) the left nostril

Table 2 provides the results for the 0.5 and 2 mm droplets (representative of the minimum and maximum diameters expected) exiting the left and right nostrils. The absolute velocity at point of impact with the ground from an initial height of 1.7 m for both droplets from both nostrils is comparable to velocities experienced from blood drops formed by passive dripping (<7 m/s), but lower than the drop velocities typical of cast-off (1.5-20 m/s), impact (1.5-30 m/s) and gunshot (15-45 m/s) [13, 14]. The initial velocity difference between the nostrils is shown to have minimal effect on the final impact velocity with the ground plane for both droplet sizes. This implies that the gravitational acceleration after the drops leave the jet has the most influence and the droplets have reached terminal velocity before they reach the ground plane (1.7 m below the nostril). The difference in exit velocity does however affect the impact location of the droplet in the ground plane especially for the 0.5 mm drop as shown in Figure 6. Distance traversed in the ground plane is shown to increase with increased velocity. The 0.5 mm drop travels over twice as far with just a 14 % increase in initial velocity. Increase in drop size from 0.5 mm to 2 mm is shown to decrease the distance traversed in the ground plane. It can also be seen that the drops exiting the nostril actually cross paths. This happens after the drops exit the boundary of the nasal jet (the nasal jet ceases 60 mm below the nostril exit) at a distance ~200 mm below the nostril exit. This can again be attributed to the asymmetry in nasal cavity geometry which can influence the exiting jet trajectory.

	Left		Right	
Drop Size (mm)	0.5	2	0.5	2
Initial Velocity (m/s)	3.47	3.47	3.96	3.96
Impact Velocity with ground Plane (m/s)	2.09	4.85	2.09	4.85
Impact distance in the ground plane from the nostril (mm)	42.7	29.2	88.7	31.2

Table 2. 0.5mm and 2mm droplet results from the left and right nostrils. The ground plane is located 1.7m below the nostril

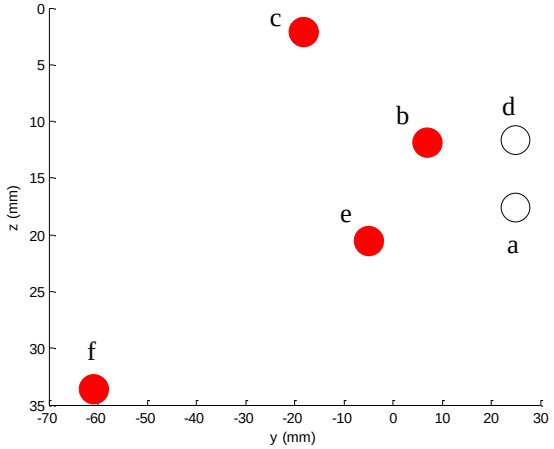

Figure 6. Drop impact location in the ground plane. Black circles signify (a) left and (d) right nostril. Red circles signify drop impact location. (b) 2mm drop and (c) 0.5mm drop from the left nostril. (e) 2mm drop and (f) 0.5mm drop from the right nostril

Conclusions

An expiration flow rate of 32 l/min in vivo produces a maximum exit velocity from the nostrils of 3.96 m/s. Exit velocity is geometry dependent, with a difference in maximum exit velocity of 0.49 m/s between the left and right nostril. Blood drops between 0.5 mm and 2 mm reach terminal velocity when ejected from a height of 1.7m, therefore exit velocity does not affect impact velocity. It does however influence impact location. Drop size affects both impact location and impact velocity. Compared to the 2 mm drop, the 0.5 mm drop had a reduced impact velocity, but its impact location in the ground plane was further from the nostril exit. This data can be used in conjunction with bloodstain impact diameters to help ascertain the location of the victim when the crime was committed. At the conference further results will be presented looking at stronger expiration velocities that are representative of someone forcing air through their nasal cavity to remove blood. Increasing the number of slices used for SPIV investigation will also produce a higher resolution velocity volume increasing the accuracy of the droplet tracking. Future work will develop a model to investigate blood drops exiting the mouth as well as the nostril. This will require incorporation of compliant sections to the silicone phantom to produce a physiologically realistic representation of the lips.

References

[1] *California, vs. Simpson*. 1995, 1997, California.

[2] *California, vs. Spector*. 2007, 2008, California Court of Appeal, California Supreme Court.

[3] *Indiana, vs. Camm*. 2004, 2006, 2013, Indiana Supreme Court.

[4] *N. Carolina, vs. Petersen*. 2003, N. Carolina.

[5] *Ohio, vs. Sheppard*. 1954, Ohio, U.S. Supreme Court.

[6] *Statistics New Zealand*. [cited 2013 5 February]; Available from: http://www.stats.govt.nz/tools_and_services/tools/TableBuilder/criminal-conviction.aspx.

[7] Davidson, P.L., Taylor, M.C., Wilson, S.J., Walsh, K. & Kieser, J.K., Physical components of soft-tissue ballistic wounding and their involvement in the generation of blood backspatter. *Journal of Forensic Sciences*, 2012. **57**: p. 1339-1342.

[8] Denison, D., Porter, A., Mills, M. & Schroter, R.C., Forensic implications of respiratory derived blood spatter distributions. *Forensic Science International*, 2011. **204**(1–3): p. 144-155.

[9] Donaldson, A.E., Walker, N.K., Lamont, I.L., Cordiner, S.J. & Taylor, M.C., Characterising the dynamics of expirated bloodstain pattern formation using high-speed digital video imaging. *International Journal of Legal Medicine*, 2011. **125**(6): p. 757-762.

[10] Geoghegan, P.H., Buchmann, N.A., Spence, C.J.T., Moore, S. & Jermy, M., Fabrication of rigid and flexible refractive-index-matched flow phantoms for flow visualisation and optical flow measurements. *Experiments in Fluids*, 2012. **52**(5): p. 1331-1347.

[11] James, S.H., Kish, P.E. & Sutton, T.P., *Principles of Bloodstain Pattern Analysis*. 2005: CRC Press.

[12] Kabaliuk, N., *Dynamics of Blood Drop Formation and Flight: A Thesis Presented for the Degree of Doctor of Philosophy in Mechanical Engineering at the University of Canterbury, Christchurch, New Zealand*. 2014, University of Canterbury.

[13] Kabaliuk, N., Jermy, M.C., Morison, K., Stotesbury, T., Taylor, M.C. & Williams, E., Blood drop size in passive dripping from weapons. *Forensic Science International*, 2013. **228**(1–3): p. 75-82.

[14] Kabaliuk, N., Jermy, M.C., Taylor, M.C. & Geoghegan, P.H., Does the non-spherical shape of a spatter drop affect its trajectory? *Journal of Bloodstain Pattern Analysis*, 2013. **29**(3&4): p. 11.

[15] Spence, C., Buchmann, N. & Jermy, M., Unsteady flow in the nasal cavity with high flow therapy measured by stereoscopic PIV. *Experiments in Fluids*, 2011: p. 1-11.